Available online at www.sciencedirect.com
ScienceDirect
Colloids and Surfaces A: Physicochem. Eng. Aspects 300 (2007) 35–49
COLLOIDS AND SURFACES A
www.elsevier.com/locate/colsurfa

A lattice Boltzmann study of viscous coupling effects in immiscible two-phase flow in porous media

Andreas G. Yiotis [a,*], John Psihogios [a,b], Michael E. Kainourgiakis [a], Aggelos Papaioannou [b], Athanassios K. Stubos [a]

[a] *National Center for Scientific Research "Demokritos", Aghia Paraskevi 15310, Greece*
[b] *School of Chemical Engineering, National Technical University of Athens, Athens 15780, Greece*

Received 15 June 2006; received in revised form 30 October 2006; accepted 7 December 2006
Available online 17 December 2006

Abstract

In the present paper we study the immiscible two-phase flow in porous media using the lattice Boltzmann model proposed by He et al. [X. He, R. Zhang, S. Chen, G.D. Doolen, Phys. Fluids 11 (1999) 1143–1152]. By considering a set of appropriate boundary conditions for the density distribution function defined in that model, we account for the effect of wettability at solid–fluid interfaces and capillarity in the pores where the fluid–fluid interfaces reside. Different contact angles of the fluid–fluid interface at solid walls can be realized by taking appropriate values for the density distribution function at the solid sites of the porous domain. It is shown that the steady state contact angle is a linear function of the density value assigned to the solid sites.

The model is then applied to the study of viscous coupling effects in immiscible two-phase flow in irregular pore networks, with respect to the overall wetting saturation, the viscosity ratio and the wetting angle. Our results show that when the wetting fluid is less viscous than the non-wetting fluid then the apparent relative permeability of the non-wetting phase may take values greater than unity due to the "lubricating" effect of the wetting films that cover the solid walls. The proposed model is an ideal tool for modeling immiscible two-phase flow in porous media, due both to its ability to incorporate complicated boundary conditions at the pore walls and also capture the physical aspects of the flow in the bulk and the interfaces. Furthermore, the width of the fluid–fluid interfaces is kept less than 3–4 lattice units allowing for simulations in relatively low resolution porous lattices.

Keywords: Lattice Boltzmann; Immiscible flow; Porous media; Viscous coupling

1. Preliminaries

The flow of a single Newtonian fluid through an isotropic porous medium is macroscopically described by Darcy's law;

$$u = -\lambda \frac{\Delta P}{\ell} \tag{1}$$

where u is the superficial velocity of the fluid, defined as $u = Q/A$, Q the volumetric flux of the fluid, A the cross-section of the pore sample, $\Delta P/\ell$ the pressure gradient and λ a proportionality constant known as mobility and defined by $\lambda = k/\mu$.

μ is the dynamic viscosity of the fluid and k is the permeability of the porous medium which is independent of the fluid properties [2,3].

Darcy's law is also used to describe the simultaneous flow of two immiscible fluids in porous media. Under the assumption that each fluid moves through its own channel which is bounded by the solid walls only (negligible area of the fluid–fluid interface) and/or that the shear stress exerted from one fluid to the other at the fluid–fluid interfaces is negligibly small (Fig. 1a), then the superficial velocity of each fluid is described by;

$$\tilde{u}_i = -\frac{k_i(S_w)}{\mu_i} \nabla P_i, \quad \text{where } i = \text{w, nw} \tag{2}$$

where k_i is the effective permeability of fluid i defined by $k_i = k k_{r,i}$ and $k_{r,i}$ the relative permeability of fluid i. The subscripts w and nw denote the wetting and the non-wetting phase, respectively.

* Corresponding author. Tel.: +30 210 6503407; fax: +30 210 6525004.
E-mail address: yiotis@ipta.demokritos.gr (A.G. Yiotis).

0927-7757/$ – see front matter © 2006 Elsevier B.V. All rights reserved.
doi:10.1016/j.colsurfa.2006.12.045

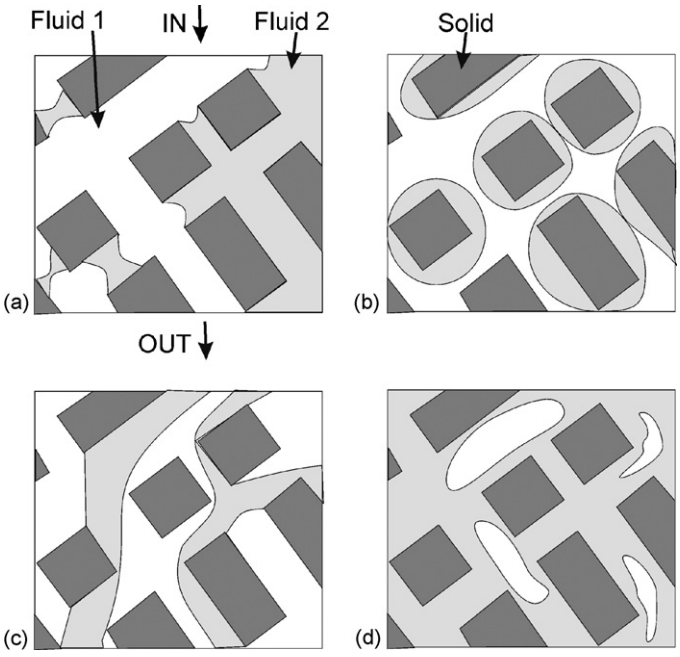

Fig. 1. Different phase distribution patterns during the immiscible two-phase flow in 2D pore networks. The figure is reproduced from Ref. [3]. (a) Each fluid moves in separate channels (pores). (b) Both fluids move in the same pores. (c) Both fluids move in the same pores but each fluid wets different portions of the solid walls. (d) Both fluids move in the same pores but the non-wetting fluid is discontinuous.

Under the assumptions described above the relative permeability $k_{r,i}$, and thus the effective permeability k_i, are both a function of the phase saturation S_w (the pore volume fraction occupied by the wetting phase), only. The relative permeability of each fluid i takes values in the region $0 \leq k_{r,i} \leq 1$.

The condition of negligible drag at the fluid–fluid interfaces is satisfied when the flow rate and the fluid viscosities are sufficiently small (namely, for small values of the capillary number $Ca = u\mu/\gamma$, where γ is the fluid–fluid interfacial tension), when the movement of the interface is controlled by capillarity and the wetting phase is contained mostly in small pores while the non-wetting phase occupies preferably larger pores (Fig. 1a) [3]. The same condition is also satisfied when the contact angle of fluid–fluid interface with the solid walls is close to 90°, so that the fluid–fluid interfaces are mostly vertical to the flow direction.

In most typical applications of immiscible flow through porous media, both fluids co-exist in most pores and there is strong viscous coupling between them. The wetting fluid moves along the solid surface and the non-wetting phase is not in contact with the solid but it flows in the central part of the void space surrounded by the wetting fluid (Fig. 1b and d).

Several authors have proposed a modification of Darcy's law (Eq. (2)) in order to account for momentum transfer across fluid–fluid interfaces and viscous coupling effects [4,5];

$$\tilde{u}_i = -\frac{k_{ii}}{\mu_i}\nabla P_i - \frac{k_{ij}}{\mu_j}\nabla P_j, \quad \text{where } i, j = \text{w, nw and } i \neq j \tag{3}$$

The permeability parameters are defined as $k_{ii} = kk_{r,ii}$ and $k_{ij} = kk_{r,ij}$. When $k_{ij} = k_{ji} = 0$ the above equations reduce to the conventional uncoupled expressions of Darcy's law (Eq. (2)).

The permeability parameter k_{ii} in Eq. (3) is equal to the permeability parameter in Eq. (2) and is function of the fluid saturation only. This parameter shows the relationship between the flow rate and the pressure gradient in phase i that would exist if the other phase j was solid. This assumption is valid only at intermediate saturations and under the conditions discussed earlier (low capillary numbers, large contact angles).

The coupled permeability parameter k_{ij} accounts for viscous coupling effects and depends on saturation among other parameters.

Eq. (3) along with an expression the for the local capillary pressure at equilibrium P_c;

$$P_{nw} - P_w = P_c(S_w) \tag{4}$$

are used to describe immiscible two-phase flow in porous media [3].

However, the coupled Eq. (3) can be expressed in a much simpler form (very similar to the uncoupled Eq. (2)) by defining an apparent relative permeability for each fluid $k_{r,i,app}$, which is a function of S_w, but also a function of the Capillary number Ca, the viscosity ratio $M = \mu_{nw}/\mu_w$ and ∇P_j. Then, the superficial velocities of the fluids are;

$$\tilde{u}_i = -\frac{kk_{r,i,app}(S_w, Ca, M, \nabla P_j)}{\mu_i}\nabla P_i, \quad \text{where } i = \text{w, nw} \tag{5}$$

and the flow rates are

$$Q_i = -Au_i, \quad \text{where } i = \text{w, nw} \tag{6}$$

In this paper we study the effect of momentum transfer across fluid–fluid interfaces on the apparent relative permeabilities of the wetting and non-wetting phases using the LB model by He et al. [1]. We propose a set of appropriate boundary conditions at the solid sites for the density distribution function of the LB model, in order to account for the effect of wettability at solid–fluid interfaces and capillarity in the pores where the fluid–fluid interfaces reside. It is shown that different contact angles of the fluid–fluid interface at solid surfaces can be realized by assigning appropriate values for the density distribution function at the solid sites of the porous domain. We use this model to study the effect of the viscosity ratio M and the contact angle θ on the apparent relative permeability curves. Our results show that the modified LB model can qualitatively capture viscous coupling effects and model the "lubricating" effect that arises when the viscosity ratio is $M > 1$.

2. Multiphase lattice Boltzmann models in porous media

Two-phase flow in porous media is a subject of significant scientific and industrial interest. It is involved in processes such as underground water flows, oil recovery, soil remediation and many more. In recent years, lattice Boltzmann models (LBM) have been used to simulate two phase flow in porous media [6,7],

and more complex two-phase processes such as viscous fingering in Hele–Shaw cells (Shaffman–Taylor instabilities) [8], Rayleigh–Taylor instabilities [9,10], Kelvin–Helmholtz instabilities [11] and the dynamics of liquid bubbles under gravity [12] among others. Such works demonstrate that the lattice Boltzmann method (LBM) is a powerful tool for the computational modeling of multiphase flow problems (see [13–16] for a review of the LB method and applications).

The LBM is a discrete method based upon the continuous Boltzmann equation. It considers a typical volume element of fluid to be composed of a collection of particles that are represented by a particle velocity distribution function for each fluid component at each grid point. The fluid particles can collide with each other as they move, possibly under applied body forces. The rules governing the collisions are designed such that the time-average motion of the particles is consistent with the Navier–Stokes equation of motion and the continuity equation.

Lattice Boltzmann (LB) models evolved form lattice gas (LG) models [17]. In Lattice Gas approaches the fluid is modeled by discrete particles moving on predefined trajectories at constant velocities. When two particles meet, they collide following predefined collision rules and trajectories. The local density and velocity is calculated by averaging the number of particles and their velocities over a large spatial volume. However, this scheme produces high local fluctuations in macroscopic quantities due to the discrete nature of the colliding particles and requires much temporal and spatial averaging to obtain accurate velocities and pressure fields. This drawback of LG models has been overcome by the consideration of particle distributions instead of single particles at each lattice site.

The growing popularity of LB models is due to the fact that they provide the means to simulate flows through and around complex solid surfaces, such as buildings, landscapes and porous materials. The boundary conditions at the solid surfaces are easily implemented in LB models through collision rules of the fluid particles with the surfaces.

Another advantage of LB models is that they are straightforward to parallelize (see for example [18]) since all variables in the discretized algorithm depend solely on nearest-neighbor information. Parallel LB models can be implemented in modern supercomputers with several hundreds of processors to simulate large-scale problems such as airflow around automobiles and airplanes, underground water and petroleum reservoir flows.

Several LB models have been applied to the study of multiphase flow through porous media. We briefly discuss the most common of these models and highlight their strengths and weaknesses when applied in porous domains. We show that the model by He et al. [1] is ideal for modeling immiscible two-phase flows in porous domains.

2.1. Gunstensen et al. model

A two-phase flow LB model was originally introduced by Gunstensen et al. [19] based on the red-or-blue Lattice Gas scheme proposed by Rothman and Keller [20]. In the Rothman and Keller model the fluid particles were colored either blue or red and the collision rules were modified to obtain surface tension between the fluids. These collision rules send particles of one color to neighboring sites containing other particles of the same color. Gunstensen et al. [19] designed a two-step two-phase collision rule that produced a locally anisotropic pressure tensor near the interface. At the first step of the model, a perturbation is added to the particle distribution near an interface, which reproduced the correct surface-tension dynamics. This addition produces surface tension at interfaces while retaining the adherence to the Navier Stokes equation in homogeneous regions. In the second step the mass is recolored to achieve zero diffusivity of one color into the other. He and Doolen [21] showed that it is difficult to incorporate microscopic interactions quantitatively in the Gunstensen model due to the heuristic modeling of particle interactions.

2.2. Shan–Chen model

Shan and Chen [22,23] proposed a LB model for multiphase flow by introducing a non-local interaction force between particles at neighboring lattice sites. The local momentum modified by the particle interaction forces is not conserved locally. However, the global momentum conservation is exactly satisfied when boundary effects are excluded. The SC model is capable of simulating both miscible and immiscible flows. The authors reported small anomalous velocities (also referred to as "spurious" velocities) in the interface region, which they attributed to the discrete nature of the model.

Several researchers have applied this model to multiphase flow in porous domains [6,7,24]. Their results were qualitatively similar to experimental data, although they did not offer good quantitative predictions. The authors argued that large lattices are required to model flow along the films of the wetting phase that form on the pore walls and obtain accurate results when the saturation of the wetting phase is less than 60%. These poor quantitative results should be also attributed to the fact that the interface in the Shan–Chen model is not sharp but it spans across several lattice units and that the porosity and lattice size were both small in these simulations.

2.3. Free energy model

A thermodynamically consistent two-phase LB model was first introduced by Swift et al. [25,26]. In this model the collision rules were chosen such that the equilibrium state corresponds to an input free energy and the bulk flow in governed by continuity, the Navier–Stokes equation and a convection-diffusion equation. Swift et al. introduced a constraint for the second momentum of the equilibrium distribution function where the pressure tensor is defined in terms of the equilibrium free energy of the fluid mixture. The model produces interfaces with a thickness of only two lattice units, which makes it ideal for modeling flows in porous media where the pore size may be only a few lattice units due to computational limitations. The original "free-energy" model is not Galilean invariant for the viscous terms in the macroscopic Navier–Stokes equation (except for the case of binary ideal fluids [21]). Several works made significant progress by

reducing the lack of Galilean invariance of the model to order u^2 [27,28].

2.4. He–Shan–Doolen model

More recently, a thermodynamically consistent LB model for the simulation of two-phase flow in the nearly incompressible limit under isothermal conditions was proposed by He et al. [1,10,29]. The interfacial dynamics, such as phase segregation and surface tension, are modeled by incorporating molecular interactions and an index function is used to track interfaces between different phases. The particle distribution function which is used in other LB models is replaced with a pressure distribution function. This change allowed for the implementation of Equations of State (EOS) in the model. The approach was based on a variation of the continuous Boltzmann equation that combined Enskog's theory for dense fluids and the mean-field theory for long-range molecular interaction. This model can describe non-ideal gas and dense fluids and was tested over several complex flows that produced Rayleigh–Taylor and Kelvin–Helmholtz instabilities at the interface. The obtained results agree well with theoretical predictions [1,10]. Recently, Lee and Lin [12] proposed a collection of consistent discretization strategies to further stabilize the model by He et al. at high density and viscosity ratios.

In this study, we consider two-phase flow in irregular pore networks using the He et al. model [1], where the interface thickness is maintained between 3 and 4 lattice units. By considering a set of appropriate boundary conditions for the particle distribution function at solid sites we account for the effect of wettability at solid–fluid interfaces. We show that different contact angles can be realized by taking appropriate density values at the pore walls. The minimum pore size in our simulations is 10 lattice units in 3D simulations and 20 lattice units in 2D simulations, in order to reduce the effect of interface thickness in our results [30]. We study the effect of the viscosity ratio M and the contact angle θ on the apparent relative permeability curves. Our results show that the modified LB model can qualitatively capture viscous coupling effects and model the "lubricating" effect that arises when the viscosity ratio is $M > 1$.

3. Model description

In this section we briefly discuss the lattice Boltzmann model proposed by He et al. [1,29]. We first describe how the LB model accounts for particle interactions in non-ideal gases and dense fluids, and then we show how the model is extended to account for two-phase flow by considering an appropriate Equation of State. We finally propose a set of boundary condition for the density distribution function at the solid sites to account for the effect of wettability.

3.1. Single phase model for non-ideal gases and dense fluids

The Boltzmann equation with the Bhatnagar-Gross-Krook (BGK) collision approximation [31] which applies for rare gases reads;

$$\frac{\partial f}{\partial t} + \tilde{\xi} \cdot \frac{\partial f}{\partial \tilde{r}} + \tilde{F} \cdot \frac{\partial f}{\partial \tilde{\xi}} = -\frac{1}{\tau}(f - f^{\mathrm{eq}}) \tag{7}$$

where $\tilde{F}$ is an external force (body force), i.e., gravity, $\tilde{\xi}$ the local velocity vector of the fluid particles, r the position vector of the particles and f is the particle density distribution function, which follows a Maxwell–Boltzmann distribution at thermodynamic equilibrium;

$$f^{\mathrm{eq}}(\tilde{r}, \tilde{\xi}) = \rho(\tilde{r}) \left[\frac{m}{2\pi k T(\tilde{r})}\right]^{3/2} \exp\left(-\frac{m(\tilde{\xi} - \tilde{u}(\tilde{r}))^2}{2kT(\tilde{r})}\right) \tag{8}$$

$\tilde{u}$ is the macroscopic velocity vector of the fluid.

He et al. [29] proposed a LB model for non-ideal gases (long distance molecular interactions). They argued that the same forcing term F, which was used to account for body forces could also account for particle interactions, such as Van der Waals forces.

They accounted for both the intermolecular attractions in non-ideal gases and the exclusion volume of molecules in dense fluids. Using a mean field approximation they found that the attractive force as a function of fluid density is;

$$\tilde{F}_{\mathrm{attr}} = -\nabla(-2a\rho - \kappa\nabla^2\rho) \tag{9}$$

When the overall molecular volume of a fluid becomes comparable with the volume of the fluid container, then the space available for the motion of each molecule is reduced significantly. The collision probability is significantly different from the collision probability in a rare gas due to the volume excluded by the molecules.

Chapman and Cowling (chap. 16, Eq. 16.32.4) [32] showed that for dense fluids the collision operator in Eq. (7) should be modified to account for the total volume of molecules and the following term should be added to the collision term of the LB equation

$$-f^{\mathrm{eq}} b\rho\chi(\tilde{\xi} - \tilde{u}_0) \cdot \nabla \ln(\rho^2\chi) \tag{10}$$

where b is a function of the molecular volume (given by $b = 2\pi\sigma^3/3m$, where σ is the effective diameter of the molecule and m is the mass of a single molecule). χ is the increase in collision probability due to the increase in fluid density. χ is equal to 1 for rare gases and greater than 1 for dense fluids.

For dense fluids the volume of the molecules becomes comparable to the volume occupied by the gas. Therefore, the space where the center of a molecule is allowed to lie is reduced and the collision probability is increased. This is called the exclusion volume effect and leads to an increase in the collision probability by the factor χ, which is a function of position. The factor χ is an increasing function of the local density ρ.

The above term accounts only for binary collisions between hard spheres (the same as in rare gases where the BGK approximation holds). These collisions are also instantaneous. The space volume occupied by the molecules increases significantly the collision probability.

By taking that $\partial f/\partial\tilde{\xi} \approx \partial f^{\mathrm{eq}}/\partial\tilde{\xi} = -f^{\mathrm{eq}}(m(\tilde{\xi} - \tilde{u})/kT) = -f^{\mathrm{eq}}((\tilde{\xi} - \tilde{u})/RT)$ and by adding the exclusion volume term

(10) to the collision operator, Eq. (7) reads;

$$\frac{\partial f}{\partial t} + \tilde{\xi}\cdot\frac{\partial f}{\partial \tilde{r}} = -\frac{1}{\tau}(f - f^{\mathrm{eq}}) - f^{\mathrm{eq}} b\rho\chi(\tilde{\xi}-\tilde{u})\cdot\nabla\ \ln(\rho^2\chi) + f^{\mathrm{eq}}\frac{\tilde{F}\cdot(\tilde{\xi}-\tilde{u})}{RT} \tag{11}$$

By combining Eqs. (9) and (11), the continuous Boltzmann equation for non-ideal gases and dense fluids reads;

$$\frac{\partial f}{\partial t} + \tilde{\xi}\cdot\frac{\partial f}{\partial \tilde{r}} = -\frac{1}{\tau}(f - f^{\mathrm{eq}}) + f^{\mathrm{eq}}\frac{\tilde{F}'\cdot(\tilde{\xi}-\tilde{u})}{RT} \tag{12}$$

where

$$\tilde{F}' = \rho\nabla(2\alpha\rho + \kappa\nabla^2\rho) - b\rho^2 RT\chi\nabla\ \ln(\rho^2\chi) \tag{13}$$

The first term of Eq. (13) comes from the intermolecular attraction and the second term comes from the exclusion-volume effect. The parameters α and b are related to the intermolecular pair-wise potential.

This expression for the forcing term, which was first proposed by He et al. [29], will be used in this study to account for the interaction of the fluid particles with the pore walls.

3.2. Two-phase model

Based on the above single phase model, He et al. [1] proposed a lattice Boltzmann model for two phase flow in the nearly incompressible limit by considering a pressure distribution function along with the density distribution function of other LB models. The consideration of a pressure distribution function allows for appropriate EOS to be implemented in the LB model in order to describe two-phase flow dynamics. The bulk density of the fluids remains approximately constant in this model. The interfacial dynamics, such as phase segregation and surface tension, are modeled through molecular interactions. The interfacial thickness is maintained at 3–4 lattice units without any artificial "recoloring" step (like in the Gunstensen et al. model [19]). This makes it ideal for modeling two-phase flow in porous media where the pore size can be only a few lattice units due to computational limitations.

Using a mean-field approximation for intermolecular attraction and following the treatment of the exclusion-volume effect by Enskog, the effective molecular attraction force is described by Eq. (13).

The terms in Eq. (13) can be conveniently rearranged as follows in order to implement the forcing term in Eq. (7);

$$\begin{aligned}\tilde{F}' &= 2\alpha\rho\nabla\rho + \kappa\rho\nabla\nabla^2\rho - b\rho^2 RT\chi\nabla(2\ \ln(\rho) + \ln(\chi)) \\ &= \alpha\nabla\rho^2 + \kappa\rho\nabla\nabla^2\rho - b\rho^2 RT\chi\left(\frac{2}{\rho}\nabla\rho + \frac{1}{\chi}\nabla\chi\right) \\ &= \kappa\rho\nabla\nabla^2\rho - \nabla(b\rho^2 RT\chi - \alpha\rho^2)\end{aligned} \tag{14}$$

The intermolecular force F' can then be expressed as;

$$\tilde{F}' = -\nabla\psi + \tilde{F}_{\mathrm{s}} = -\nabla\psi + \kappa\rho\nabla\nabla^2\rho \tag{15}$$

where F_{s} is the force associated with the surface tension and ψ the function of the density given by $\psi = b\rho^2 RT\chi - \alpha\rho^2$ and is related to the pressure by $P = \psi(\rho) + \rho RT$.

By considering an appropriate EOS to describe the macroscopic pressure as a function of the local density, the LB model can simulate two-phase flow.

Assuming that the pressure of non-ideal fluids is described by the Carnahan–Starling EOS [33];

$$p = \rho^2 RT\frac{4-2\rho}{(1-\rho)^3} - a\rho^2 + \rho RT \tag{16}$$

then

$$\psi(\rho) = \rho^2 RT\frac{4-2\rho}{(1-\rho)^3} - a\rho^2 \tag{17}$$

Note that for $\alpha > 10.601RT$, Eq. (16) has three roots that produce the same pressure p. Two of them are mechanically stable ($\mathrm{d}p/\mathrm{d}V < 0$) and one is unstable ($\mathrm{d}p/\mathrm{d}V > 0$). The unstable root lies between the two stable roots and induces phase separation. If the temperature exceeds the critical value $T \geq a/10.601R$ then the intermolecular attraction is weak and the fluid exists in a single stable phase (supercritical).

He et al. argued that the direct solution of Eq. (12) is difficult due to the calculation of the intermolecular force. To overcome this problem they proposed a new pressure distribution function defined as $g = fRT + \psi(\rho)\Gamma(0)$, where $\Gamma(\tilde{u})$ is a function of the macroscopic velocity u.

The evolution equation for g is;

$$\frac{\mathrm{D}g}{\mathrm{D}t} = RT\frac{\mathrm{D}f}{\mathrm{D}t} + \Gamma(0)\frac{\mathrm{D}\psi(\rho)}{\mathrm{D}t} \tag{18}$$

The material derivative for incompressible fluids is;

$$\frac{\mathrm{D}\psi(\rho)}{\mathrm{D}t} = \frac{\partial\psi(\rho)}{\partial t} + (\tilde{\xi}-\tilde{u})\cdot\nabla\psi(\rho) = (\tilde{\xi}-\tilde{u})\cdot\nabla\psi(\rho) \tag{19}$$

and finally;

$$\frac{\mathrm{D}g}{\mathrm{D}t} = -\frac{g-g^{\mathrm{eq}}}{\lambda} + (\tilde{\xi}-\tilde{u})\cdot [\Gamma(\tilde{u})(\tilde{F}_{\mathrm{s}} + \tilde{G}) - (\Gamma(\tilde{u}) - \Gamma(0))\nabla\psi(\rho)] \tag{20}$$

He et al. used Eq. (12) to calculate the density field only, so they removed the forces which have no effect on mass conservation. They retained however the intermolecular force $\nabla\psi(\rho)$ which is essential in phase separation. They introduced an index function φ which also satisfies Eq. (16) and they discretized Eq. (12) for the index function f;

The discrete LB model by He et al. reads;

$$\begin{aligned}&f_i(\tilde{x} + \tilde{\mathrm{e}}_i\delta t, t + \delta t) \\ &= f_i(\tilde{x}, t) - \frac{f_i(\tilde{x}, t) - f_i^{\mathrm{eq}}(\tilde{x}, t)}{\tau} \\ &\quad - \frac{2\tau - 1}{\tau}\frac{(\tilde{\mathrm{e}}_i - \tilde{u})\cdot\nabla\psi(\varphi)}{RT}\Gamma_i(\tilde{u})\delta t\end{aligned} \tag{21}$$

and the discretized Eq. (20) is;

$$g_i(\tilde{x}+\tilde{e}_i\delta t, t+\delta t) = g_i(\tilde{x},t) - \frac{g_i(\tilde{x},t)-g_i^{eq}(\tilde{x},t)}{\tau} - \frac{2\tau-1}{\tau}(\tilde{e}_i-\tilde{u})\cdot [\Gamma_i(\tilde{u})(\tilde{F}_s+\tilde{G}) - (\Gamma_i(\tilde{u})-\Gamma_i(0))\nabla\psi(\rho)]\delta t \quad (22)$$

where $\tilde{e}_i = \tilde{\xi}_i$.

The local index function φ is calculated form the first momentum of the distribution function f,

$$\varphi(x,y,z) = \sum_i f_i(x,y,z) \quad (23)$$

and the pressure and velocity are calculated from the first and second momentums of the distribution function g, respectively;

$$p(x,y,z) = \sum_i g_i(x,y,z) - \frac{1}{2}\tilde{u}(x,y,z)\cdot\nabla\psi(\rho)\delta t \quad (24)$$

$$\rho(x,y,z)RT\tilde{u}(x,y,z) = \sum_i \tilde{e}_i g_i(x,y,z) + \frac{RT}{2}(\tilde{F}_s+\tilde{G})\delta t \quad (25)$$

Different density values can be realized through a linear dependence of the phase density ρ with the phase index function φ;

$$\rho(\varphi) = \rho_{low} + \frac{\varphi-\varphi_{low}}{\varphi_{high}-\varphi_{low}}(\rho_{high}-\rho_{low}) \quad (26)$$

where ρ_{low}, ρ_{high}, φ_{low}, φ_{high} are the low and high values of density and the phase index function, respectively.

3.3. Capillary effects

The original LB model developed by He et al. [1] does not account for intermolecular forces between fluid and solid molecules at the fluid–solid interface. The bounce-back boundary condition is applied to all fluid particles when they collide with a solid wall. The bounce-back boundary condition conserves the momentum of the fluid particles prior to and after the collision with the pore walls. Although this scheme is first-order accurate with respect to the particle speed, it is used in most LB models due to its simplicity and because only nearest-neighbor information is required at each site of the computational domain.

In this paper we extend this LB model to the more general case of a three-phase system including a solid in contact with a liquid and its vapors (Fig. 2). For a complete description of this problem both the pair-wise intermolecular potentials and their range are required. We follow the assumption by Rowlinson and Widom [34] that the solid is made up of rigid molecules of given density. We should note here that this is a only a crude estimate of the true chemical constitution of the solid and it is adopted in our approach in order to take advantage of the mean field approximation for the intermolecular potential by Rowlinson and Widom [34].

Based on this assumption, we account for attracting (adhesive) forces between fluid particles and molecules of the solid surface by assigning an "effective" value for the density of the solid sites in the range between ρ_{gas} and ρ_{liq}, depending on whose phase's molecules are attracted stronger by the molecules of the solid surface. The density assigned to the solid lattice sites enters the calculations through Eq. (15) for the force due to surface tension F_s. This boundary condition can be used to modify the contact angle of the interface at the solid surface.

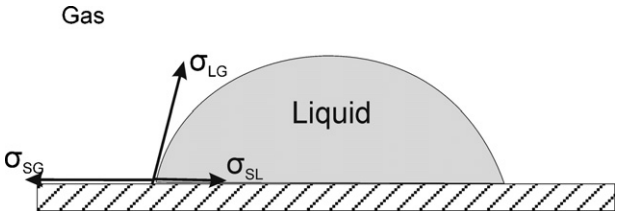

Fig. 2. Schematic representation of the interfacial tensions at the intersection of the liquid–gas, gas–solid and liquid–solid interfaces.

The effect of the assigned effective density value is demonstrated by considering a square 'droplet' of the liquid phase located between two parallel solid plates (Fig. 3). The upper and bottom sides of the droplet are in direct contact with the solid plates and the other two sides are in contact with the gas phase. A value in the range between ρ_{gas} and ρ_{liq} is assigned to the solid sites (solid density) and the system is left to reach equilibrium. Fig. 3 shows the equilibrium contact angle of the liquid–gas interfaces for various values of the solid density. As the value for the solid density ρ_s is changed from ρ_{liq} to ρ_{gas}, the system changes from liquid-wet (upper left part of Fig. 3) to gas-wet (lower right part of Fig. 3).

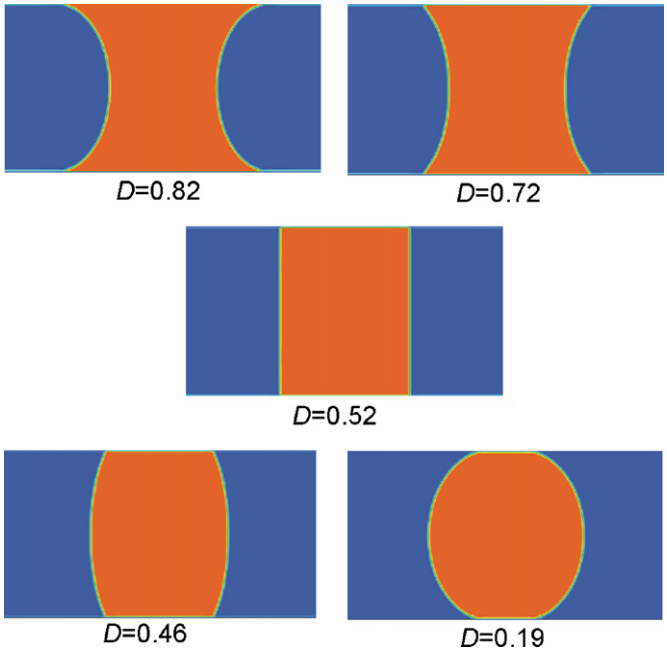

Fig. 3. Effect of the normalized solid density $D=(\rho_s-\rho_{gas})/(\rho_{liq}-\rho_{gas})$ on the wetting angle for a liquid droplet located between two parallel plates at equilibrium. The system changes from strongly liquid-wet (upper left image) to strongly gas-wet (lower right image) as the density of the solid walls decreases from ρ_{liq} to ρ_{gas}. The size of the computational domain is 300×300. $\kappa=10^{-5}$.

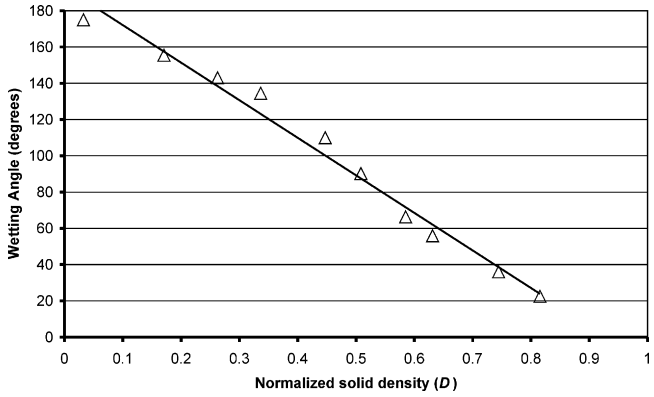

Fig. 4. Wetting angle (°) vs. the normalized solid density $D = (\rho_s - \rho_{gas})/(\rho_{liq} - \rho_{gas})$. The wetting angle exhibits a linear dependence on the solid density. $10^{-2} \leq \kappa \leq 10^{-5}$.

The contact angle exhibits a linear dependence to the normalized solid density;

$$D = \frac{\rho_s - \rho_{gas}}{\rho_{liq} - \rho_{gas}} \tag{27}$$

as shown in Fig. 4.

Approaches similar to the one described above are also used by Bekri and Adler [35] for the Gunstensen LB model and also in the original LB model by Shan and Chen [22] through the fluid–solid interaction potential.

When the solid surface is very long compared to the size of the liquid bubble and when $D = 1$, namely when the solid is strongly water-wet, we expect that the liquid bubble will soon become very thin and will eventually break-up so that both solid plates are fully covered by a liquid film. The thickness of the liquid film is the same on both plates. The evolution of such a bubble is shown in Fig. 5.

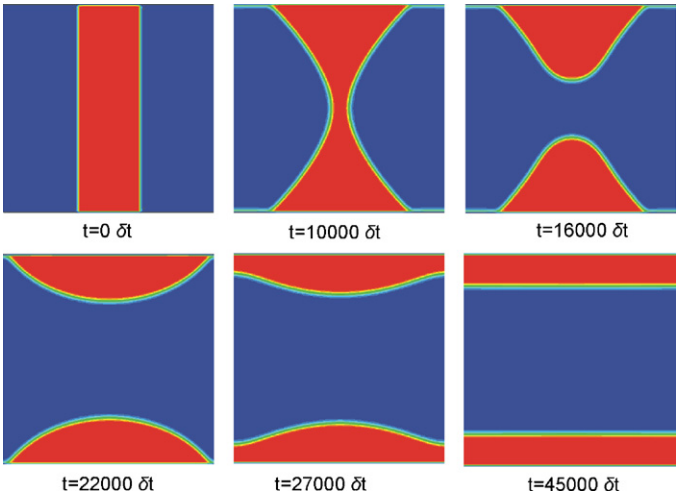

Fig. 5. Evolution of a liquid bubble (colored red) located between two parallel plates when the solid is strongly liquid-wet ($D \to 1$) and the size of the bubble is small compared to the length of the solid surface. The size of the computational domain is 100×100. $D = 0.75$ and $\kappa = 0.1$. (For interpretation of the references to colour in this figure legend, the reader is referred to the web version of the article.)

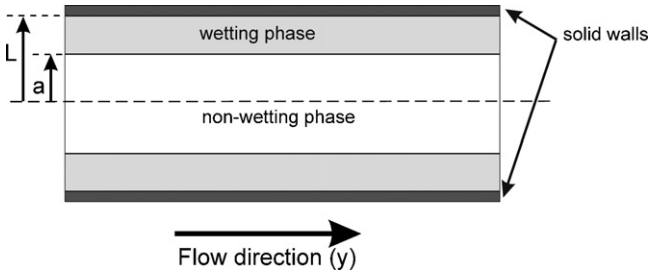

Fig. 6. Schematic of immiscible two phase flow between parallel plates. The wetting phase flows along the solid walls, while the non-wetting phase occupies the central region of the flow.

4. Viscous coupling during co-current flow in a 2D channel

In immiscible two-phase flow in porous media, the wetting phase typically covers the surface of the solid where it flows in the form of films (Figs. 1b and 5). The non-wetting phase is not in direct contact with the solid surface but it flows between the films of the wetting phase. The velocity of the non-wetting phase through the pores is affected by the viscosity ratio of the fluids defined as $M = \mu_{nw}/\mu_w$.

This is better demonstrated through the following study of immiscible two-phase co-current flow through two parallel plates. The length of the plates is infinite in the direction of the flow and periodic boundary conditions apply at the sides vertical to the direction of the flow. No-slip boundary conditions apply at the plates. Both fluids have the same kinematic viscosity ν but different densities ρ which produces different dynamic viscosities $\mu = \rho\nu$.

For a given value of the wetting saturation S_w, we take the wetting phase flowing along the parallel plates in the region $a < |x| < L$ (namely, in two films with same thickness $L–a$), and the non-wetting phase flowing in the central region $0 < |x| < a$, where $S_w = (L - a)/L = (1 - a)/L$ and $S_{nw} = a/L$ (Fig. 6).

We study the velocity profile at a cross-section vertical to the direction of the flow. Assuming a Poiseuille-type flow, the analytical solution for the velocity profile between the parallel plates is;

$$u(x) = \frac{\Delta P}{2\ell\eta_w}(L^2 - x^2) = \frac{F}{2\nu_w\rho_w}(L^2 - x^2) \text{ in the wetting phase region, } a < |x| < L, \tag{28}$$

and

$$u(x) = \frac{\Delta P}{2\ell\eta_w}(L^2 - a^2) + \frac{\Delta P}{2\ell\eta_{nw}}(a^2 - x^2) = \frac{F}{2\nu_w\rho_w}(L^2 - a^2) + \frac{F}{2\nu_{nw}\rho_{nw}}(a^2 - x^2)$$

in the non-wetting phase region, $0 < |x| < a$, (29)

where ν_w, ν_{nw}, ρ_w, ρ_{nw} are the kinematic viscosities and densities of the wetting and non-wetting phases, respectively. The

pressure gradient in the direction of the flow is taken equal to F, i.e., $\Delta P/\ell = F$. The pressure gradient is the same in both phases but the dynamic viscosity produces different average velocities in each phase. So the average volumetric rate is different in each phase.

The relative permeability of each phase is defined in terms of the superficial velocity of the fluid particles across a cross-section perpendicular to the flow direction (y);

$$k_{\mathrm{r,w}}(S_{\mathrm{w}}) = \frac{\int_{|x|=a}^{L} v_{\mathrm{w}}\,\mathrm{d}x}{\int_{|x|=0}^{L} v_{\mathrm{w}}\,\mathrm{d}x}, \qquad k_{\mathrm{r,nw}} = \frac{\int_{|x|=0}^{a} v_{\mathrm{nw}}\,\mathrm{d}x}{\int_{|x|=0}^{L} v_{\mathrm{nw}}\,\mathrm{d}x} \tag{30}$$

It can be easily shown using Eqs. (28)–(30) that the relative permeabilities as a function of the wetting saturation is given by (see the Appendix for more details)

$$k_{\mathrm{r,w}} = \frac{1}{2}S_{\mathrm{w}}^2(3 - S_{\mathrm{w}}),$$

$$k_{\mathrm{r,nw}} = S_{\mathrm{nw}}\left[\frac{3}{2}M + S_{\mathrm{nw}}^2\left(1 - \frac{3}{2}M\right)\right] \tag{31}$$

Eq. (31) shows that the relative permeability of the wetting phase between two parallel plates is a function of the wetting saturation S_{w} only. However, the relative permeability of the non-wetting phase is a function of both the wetting saturation and the viscosity ratio M.

When $M \ll 1$, namely when the viscosity of the wetting phase is much larger than the viscosity of the non-wetting phase then $k_{\mathrm{r,nw}} = S_{\mathrm{nw}}^3 = (1 - S_{\mathrm{w}})^3$ and the relative permeability is always less than 1. When $M > 1$, then the relative permeability of the non-wetting phase is a function of both S_{w} and M, and it may take values greater than 1 (see Fig. 10).

4.1. Relative permeabilities when $M < 1$

Using the LB model presented in the previous section we solve for the velocity profile in the slit in order to calculate the relative permeabilities of both phases as a function of the wetting saturation and the viscosity ratio M.

We first consider the case where $M < 1$, namely when the viscosity of the wetting phase is greater than the viscosity of the non-wetting phase. Fig. 7 shows the velocity profile for $M = 0.1$. Although both phases are subject to the same pressure gradient, the non-wetting phase accelerates faster than the wetting phase because it is less viscous. The velocity profile calculated with the LB model is in very good agreement with the analytical solution.

Fig. 8 shows the relative permeabilities as a function of the wetting phase saturation. The relative permeability of both phases is less than 1 when $M < 1$, as expected from Eq. (31).

4.2. Relative permeabilities when $M > 1$

When $M > 1$, the velocity of the non-wetting phase is significantly affected by the saturation of the wetting phase. Fig. 9 shows the velocity profile for $M = 10$. In this case the viscosity of the wetting phase is smaller than the viscosity of the non-wetting phase. The agreement between the analytical solution

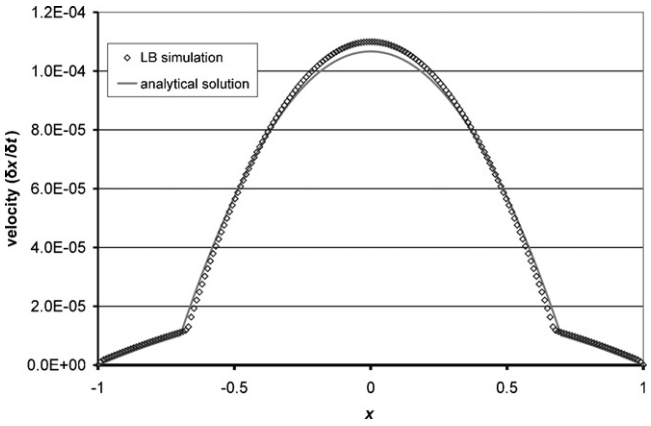

Fig. 7. Steady state velocity profile perpendicular to the direction of the flow when the more viscous fluid is the wetting phase. $M = 0.1$, $F = 1.0\,\mathrm{e}^{-10}$, $v = 0.1$, $\rho_{\mathrm{w}} = 0.25$, $\rho_{\mathrm{nw}} = 0.02514$, and $\kappa = 0$.

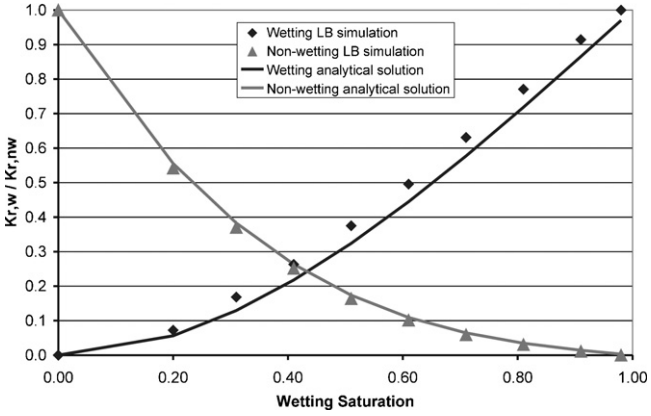

Fig. 8. Calculated relative permeabilities for the wetting and non-wetting phases in a slit when $M = 0.1$. Also shown the analytical solutions for both phases.

and numerical results obtained using the LB model by He et al. is very satisfactory.

The relative permeabilities of both phases as a function of the wetting saturation S_{w} are shown in Fig. 10. The LB model shows that the relative permeability of the wetting phase is inde-

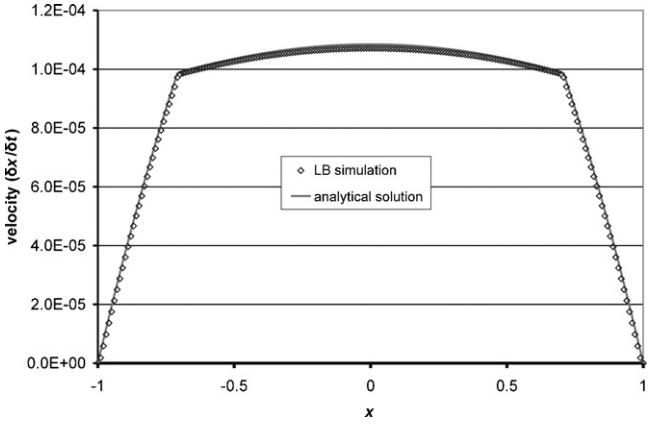

Fig. 9. Steady state velocity profile perpendicular to the direction of the flow when the less viscous fluid is the wetting phase. $M = 10$, $F = 1.0\,\mathrm{e}^{-10}$, $v = 0.1$, $\rho_{\mathrm{w}} = 0.25$, $\rho_{\mathrm{nw}} = 0.02514$, and $\kappa = 0$.

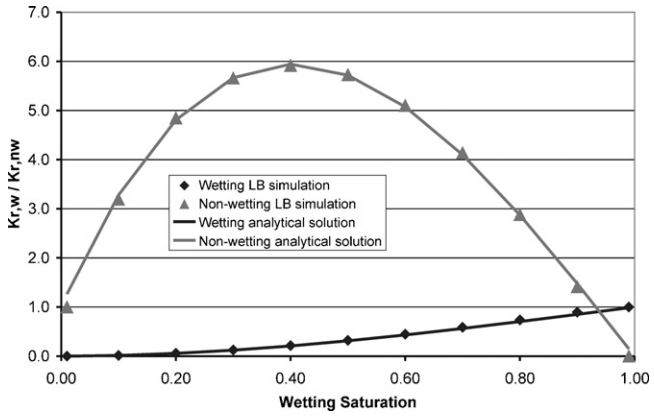

Fig. 10. Calculated relative permeabilities for the wetting and non-wetting phases in a slit when $M = 10$. Also shown the analytical solutions for both phases. The permeability of the non-wetting phase in a slit where both phases coexist is typically greater than the relative permeability of the single phase flow of the non-wetting phase ($S_{nw} = 1$) due to the "lubricating" effect of the wetting phase at the solid walls [36]. The relative permeability of the wetting phase is not affected by the viscosity ratio M.

pendent of the viscosity ratio. The relative permeability of the non-wetting phase is typically greater than the absolute permeability of the single-phase flow of the non-wetting component flowing between two parallel plates for low to intermediate values of the wetting fluid saturation. This is the well-known "lubricating" effect [36], which is captured very satisfactorily by our simulations. The numerical results are in good agreement with the analytical solution.

Fig. 11 shows the relative permeabilities for $M = 0.1$, $M = 1$, $M = 3$ and $M = 10$. The error of the LB simulations is less than 15% for all values of M. The maximum error appears for very low and very high values of S_w, while for intermediate values the error is practically negligible.

The relative permeability of the wetting phase is practically independent of the viscosity ratio as expected (Eq. (31)). However, the relative permeability of the non-wetting phase is strongly dependent on the viscosity ratio M. When $M \ll 1$, namely when the viscosity of the wetting phase is much larger

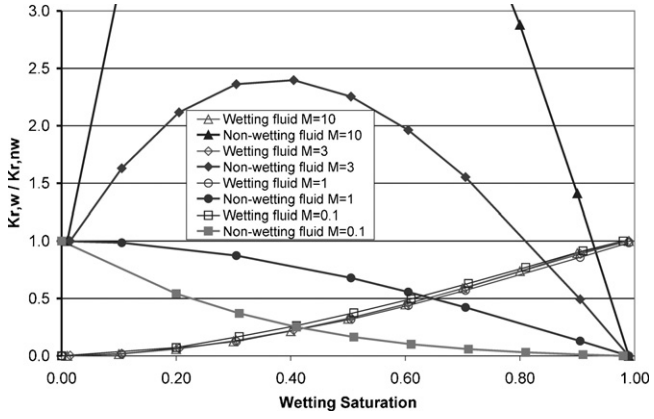

Fig. 11. Calculated relative permeabilities for the wetting and non-wetting phases in a slit for various values of the viscosity ratio M. $F = 1.0\,e^{-10}$, $v = 0.1$, and $\kappa = 0$.

than the viscosity of the non-wetting phase then $k_{r,nw} = S_{nw}^3 = (1 - S_w)^3$ and the relative permeability is always less than 1. When $M > 1$, then the relative permeability of the non-wetting phase is a function of both S_w and M, and it may take values greater than 1 (Fig. 10).

5. Flow through pore networks

The simplified Poiseuille-type flow considered in the previous section offers some insight in viscous coupling in a single channel. In this section we consider the more complicated problem of two-phase flow in a porous medium. The porous medium is represented by 2D and 3D pore networks of N^2 square or N^3 cubic solid and void (pore space) blocks. The size of each block is n^d lattice units (δx) and so the size of the computational domain is $L^d = (N \times n)^d$ lattice units, where d is the dimensionality of the pore network. The blocks are randomly distributed in space so that the probability of finding a void block at each one of the N^d positions in the network is equal to ε, where ε is the porosity of the network. The probability of finding a solid block is $1 - \varepsilon$.

Initially, we consider that the liquid and gas phases also reside in blocks of size n^d lattice units distributed at random in the void blocks with a probability S_w for the wetting phase and $1 - S_w$ for the non-wetting phase, where S_w is the wetting saturation.

The pore network is subject to periodic boundary conditions in all directions. We calculate the steady state superficial velocity

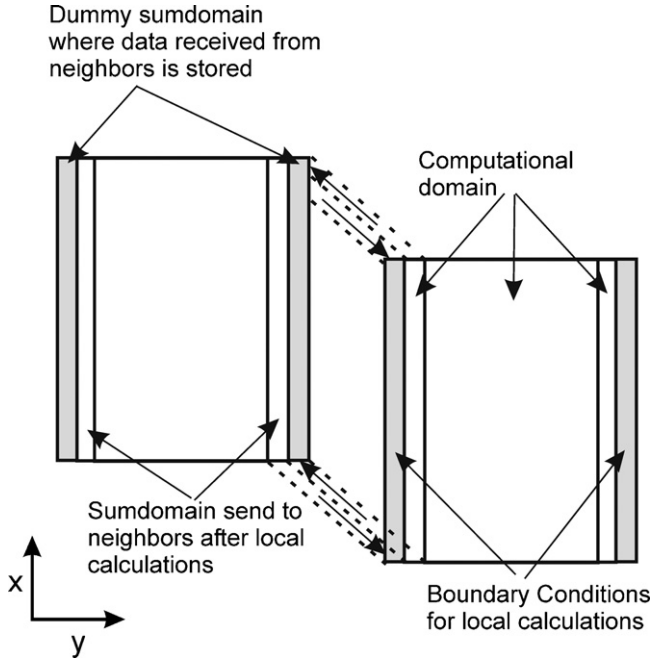

Fig. 12. Schematic of the domain decomposition in our algorithm. The computational domain for each processor is shown in white color. At the boundaries of the computational subdomains, the data calculated at the previous time step is stored in dummy subdomains (where no calculations take place), shown in grey color. The dummy subdomains serve as boundary conditions for the local calculations at the current time step. The computational domain (two-dimensional arrays) is decomposed in the y-direction in order to take advantage of Fortran's column-major storage of multi-dimensional array elements.

of each phase in order to estimate the relative permeabilities as a function of the wetting saturation and the viscosity ratio M.

The lattice Boltzmann model described in Section 3 is parallelized for implementation on distributed memory computers using the Message Passing Interface (MPI) libraries (see Pacheco [37] for a review of MPI programming). The computational domain (two- and three-dimensional arrays) is decomposed in the y-direction in 2D pore networks and in the z-direction in 3D pore networks in order to take advantage of Fortran's column-major storage of multi-dimensional array elements. This scheme ensures that array elements exchanged across processors with MPI are located in continuous memory blocks (Fig. 12).

The numerical simulations terminated when the average velocity of both phases reached a steady state. This typically required more than 300,000 time steps for a body force of $G = 10^{-7}$.

6. Results and discussion

A series of numerical simulations were performed in a 2D pore network with porosity $\varepsilon = 0.77$ and a 3D pore network with porosity $\varepsilon = 0.53$ for various values of the initial wetting saturation S_w and fixed values of the wetting angle θ. The porosity was selected to be greater than 0.6 in 2D and greater than 0.3 in 3D, so that the network is percolating in all directions. For the 2D simulations, the dimension of the computational grid was 400×400 lattice units ($L = 400\delta x$) and the size of each block of solid or void was 20×20 lattice units ($n = 20\delta x$). Thus, the dimension of the pore network was 20×20 blocks ($N = 20$). For the 3D simulations, the computational domain was $100 \times 100 \times 100$ lattice units ($L = 100\delta x$) and the size of each block of solid or void was $10 \times 10 \times 10$ lattice units ($n = 10\delta x$). The size of the pore network was $10 \times 10 \times 10$ blocks ($N = 10$).

The immiscible flow through the pore network is characterized by three dimensionless numbers; the viscosity ratio $M = \mu_{nw}/\mu_w$, the Reynolds number $Re = ud/\nu$ and the capillary number Ca, which expresses the ratio of viscous forces to capillary forces in any pore and is usually defined as $Ca = u\mu/\gamma$.

The maximum gas velocity in our simulations was $u = 10^{-3}(\delta x/\delta t)$ in the higher porosity 2D pore networks when the saturation of the less viscous phase was 100%. The applied body force was $G = 10^{-7}(\delta x/\delta t^2)$ in 2D and $G = 10^{-6}(\delta x/\delta t^2)$ in 3D pore networks.

The kinematic viscosity is $\nu = (1/3)(\tau - (1/2))(\delta x^2/\delta t)$. The dimensionless relaxation time was selected $\tau = 0.8$, therefore $\nu = 0.1(\delta x^2/\delta t)$.The maximum Reynolds number in our simulations was $\mathrm{Re} = un/\nu = 0.2$. This ensures that the flow rate is sufficiently low so that Darcy's law is valid in our pore network [2], but, at the same time, sufficiently high so that there is strong viscous coupling between the two phases.

The capillary number Ca is obtained from our simulation by taking the ratio of the body forces to the interfacial forces $Ca = G/F_s = 10^{-7}/4.25 \times 10^{-5} = 0.002$ in 2D and $Ca = 0.02$ in 3D. These are relatively high values of Ca, where the movement of the interface is controlled by viscous forces [38].

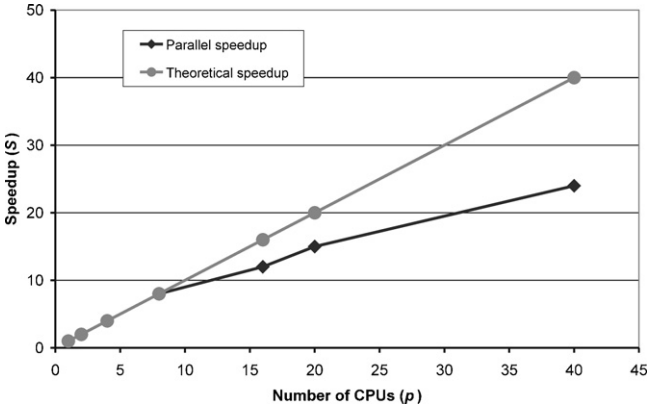

Fig. 13. Parallel speedup of our LB algorithm.

Our typical production runs were performed on 10–20 CPUs for 300,000 to 1,000,000 δt. Each numerical simulation required approximately 4–32 h, depending on the dimensionality of the pore network and the number of available CPUs.

The parallel speedup of our algorithm is shown in Fig. 13. The speedup is defined as $S(p) = t(\text{serial})/t(p)$ where $t(\text{serial})$ is the execution time of the serial code and $t(p)$ is the execution time of the parallel code on p CPU's. The parallel efficiency E of our LB code is greater than 0.8 on 20 CPU's and drops to 0.625 on 40 CPU's. The parallel efficiency is defined as $E(p) = S(p)/p$.

6.1. Wetting phase viscosity is less than non-wetting phase viscosity ($M > 1$)

We first consider the case where the viscosity of the wetting phase is less than the viscosity of the non-wetting phase, namely $M > 1$. The normalized solid density defined by Eq. (27) is taken equal to $D = 0.05$. As described in Section 3, this produces a contact angle $\theta = 175°$.

A series of numerical simulations were performed for various values of the initial wetting saturation S_w, in order to calculate phase distribution patterns and the apparent relative permeabilities. The apparent relative permeabilities are calculated through the average velocity of each phase at steady state as discussed in Section 4. The average (superficial) velocity of the flow typically reaches a steady state value after 300,000 δt, as shown in

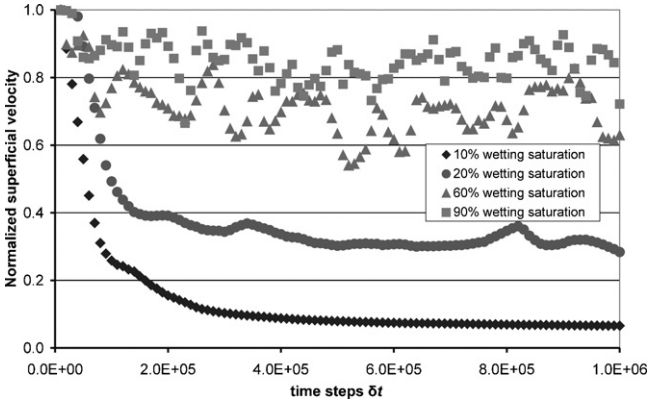

Fig. 14. Convergence of the superficial velocity of the wetting phase in our 2D simulations with respect to the elapsed time steps δt. $G = 1.0\,e^{-7}$, and $\varepsilon = 0.77$.

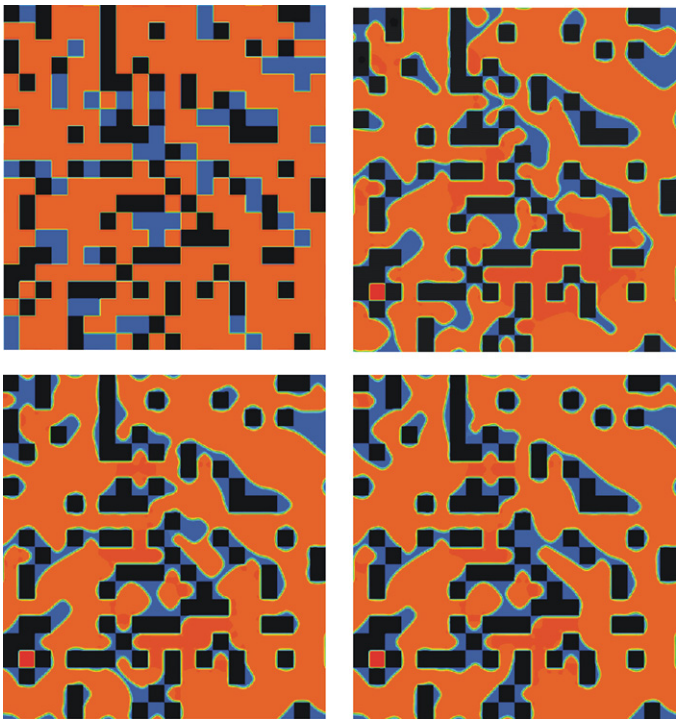

Fig. 15. Phase distribution patterns in 2D pore networks at different times ($t = 0$, 100,000, 200,000, 300,000δt) when the wetting phase is the less viscous phase (blue color) $M = 10$ at $S_w = 0.2$. The more viscous phase is shown in red color. $D = 0.05$, $\theta = 175^\circ$, $G = 1.0\,e^{-7}$, $\varepsilon = 0.77$, and $\kappa = 10^{-4}$. The wetting phase is not spanning and its permeability is equal to zero, while the non-wetting phase is spanning the whole network. (For interpretation of the references to colour in this figure legend, the reader is referred to the web version of the article.)

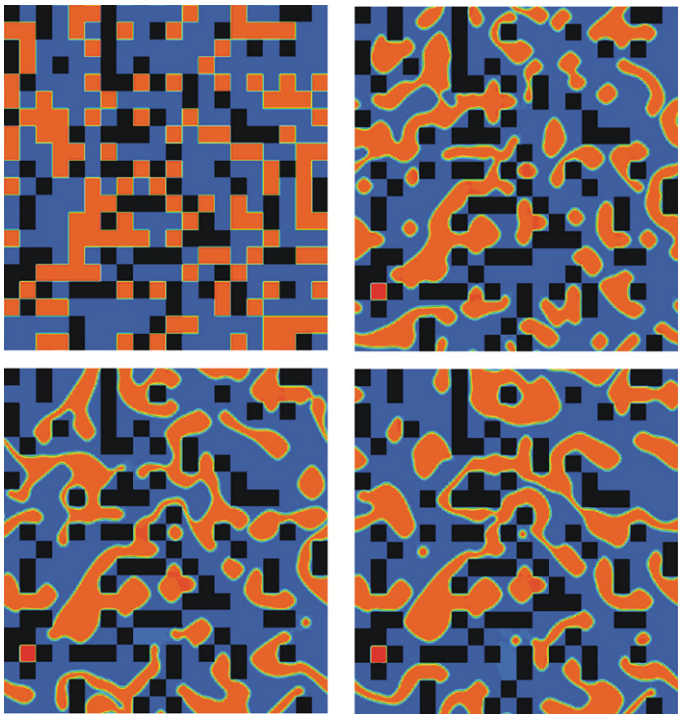

Fig. 16. Phase distribution patterns in 2D pore networks at different times ($t = 0$, 100,000, 200,000, 300,000δt) when the wetting phase is the less viscous phase (blue color) $M = 10$ at $S_w = 0.6$. The more viscous phase is shown in red color. $D = 0.05$, $\theta = 175^\circ$, $G = 1.0\,e^{-7}$, $\varepsilon = 0.77$, and $\kappa = 10^{-4}$. The non-wetting phase is still spanning most of the time, but also a significant amount of the non-wetting phase flows in large blobs. (For interpretation of the references to colour in this figure legend, the reader is referred to the web version of the article.)

Fig. 14. However, the variance of the numerical values increases significantly as the wetting saturation increases. This should be attributed to the wetting phase being less viscous than the non-wetting phase.

Fig. 15 shows the evolution of the phase distribution patterns when the wetting saturation is $S_w = 0.2$. The wetting phase (shown in blue color) covers the solid surface, while the non-wetting phase (shown in red color) forms a spanning cluster that flows among the wetting phase films. The wetting phase is practically immobile and its permeability is equal to zero since the solid blocks are not spanning the 2D pore network.

Fig. 16 shows the evolution of the phase distribution patterns when wetting phase saturation is $S_w = 0.6$. Both phases are now spanning at all times. The non-wetting phase also flows in large blobs that detach from the continuous non-wetting phase.

At high wetting phase saturations, i.e., $S_w = 0.8$ in Fig. 17, the wetting phase is continuous and the non-wetting phase becomes discontinuous. The non-wetting phase flows in the form of small blobs. These blobs are significantly accelerated due to the lubricating effect of the wetting gas phase that covers the pore walls.

This is demonstrated in Fig. 18 that shows the apparent relative permeabilities for both phases with respect to the wetting saturation when $M > 1$. For low to intermediate values of the wetting saturation, the relative permeability of the non-wetting phase is significantly larger than 1 due to the lubricating effect.

Similar results are obtained from simulations in 3D pore networks when $M > 1$. Fig. 19 shows the distribution of the wetting and non-wetting phases in the pore space when the wetting saturation is $S_w = 0.8$. The non-wetting phase is flowing through the pore-space in the form of large discontinuous blobs. Fig. 20 shows the relative permeability curves for both fluids. The apparent permeability of the non-wetting phase is greater than 1 when the wetting phase saturation is smaller than 0.7 and exhibits a maximum at approximately $S_w \approx 0.5$ for the specific pore structure.

Non-wetting phase permeabilities exceeding single phase permeabilities have been measured by Odeh [36] indicating lubrication by a thin wetting phase film covering the pore walls (Fig. 21). However, this phenomenon has not been studied in detail and the relevant literature is very limited.

Goode and Ramakrishnan [39] produced relative permeabilities of the non-wetting phase greater than 1 using a pore network model when $M > 1$. Ehrlich [40] also produced similar results using a bundle of capillary tubes model. He showed lubrication of oil by water located in the corners of the irregularly shaped tubes due to viscous coupling at the liquid–liquid interface. For $M = \mu_{oil}/\mu_{water} > 1$, the oil apparent relative permeability is greater than one over a significant range of S_w. This is in agreement with the results obtained in this study. Ehrlich also showed that water relative permeability shows little sensitivity to M, as we will also demonstrate in the next section.

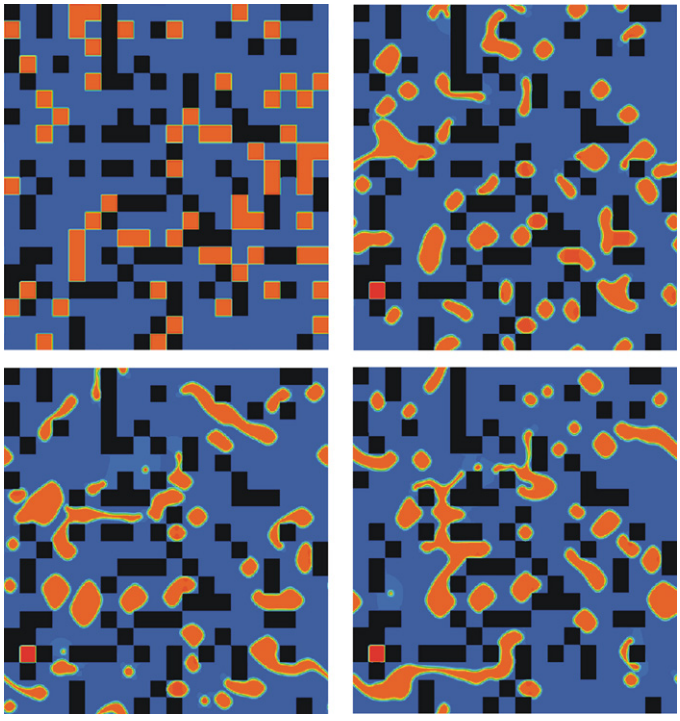

Fig. 17. Phase distribution patterns in 2D pore networks at different times ($t = 0$, 100,000, 200,000, 300,000δt) when the wetting phase is the less viscous phase (blue color) $M = 10$ at $S_w = 0.8$. The more viscous phase is shown in red color. $D = 0.05$, $\theta = 175^\circ$, $G = 1.0\,e^{-7}$, $\varepsilon = 0.77$, and $\kappa = 10^{-4}$. The wetting phase is now spanning the entire network and the non-wetting phase flows in the form of small blobs. (For interpretation of the references to colour in this figure legend, the reader is referred to the web version of the article.)

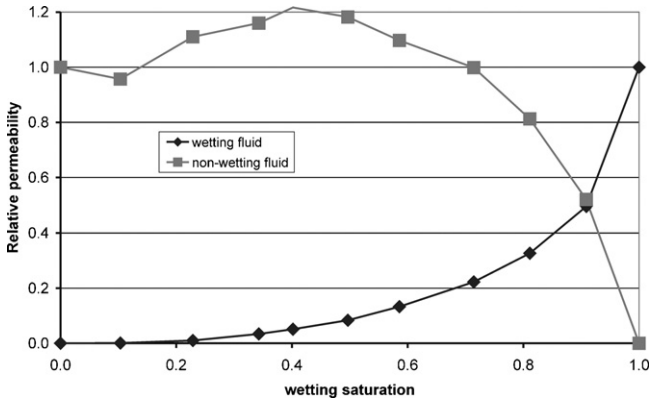

Fig. 18. Relative permeabilities in 2D pore networks when $M = 10$. $D = 0.05$, $\theta = 175^\circ$, $G = 1.0\,e^{-7}$, $\varepsilon = 0.77$, and $\kappa = 10^{-4}$. The relative permeability of the non-wetting phase is greater than 1 for intermediate values of the wetting saturation due to the "lubricating effect" at the pore walls and viscous coupling between the phases within the pores.

6.2. *Wetting phase viscosity is greater than non-wetting phase viscosity ($M < 1$)*

We also consider the case where the viscosity of the wetting phase is greater than the viscosity of the non-wetting phase, namely $M < 1$. The normalized solid density is taken equal to $D = 0.65$. This produces a contact angle $\theta = 55^\circ$.

Fig. 22 shows the evolution of the phase distribution patterns when the saturation of the less viscous non-wetting phase is $S_{nw} = 0.2$ and $M = 0.1$. The wetting phase (red) covers most of the solid surface, while the non-wetting gas phase flows in the form of small blobs and is not spanning the pore network.

Fig. 23 shows the evolution of the phase distribution patterns when the gas saturation is $S_{nw} = 0.6$ and $M = 0.1$. The wetting liquid phase covers most of the solid surface and it flows in the form of large blobs that become detached form the solid walls. Due to the relatively large value of the contact angle (close to 90°), the solid walls are not entirely covered by the wetting phase, as in Section 6.1. Both phases coexist in the pore channels and both are in contact with the solid surface, although the solid surface is mostly covered by the more viscous wetting phase.

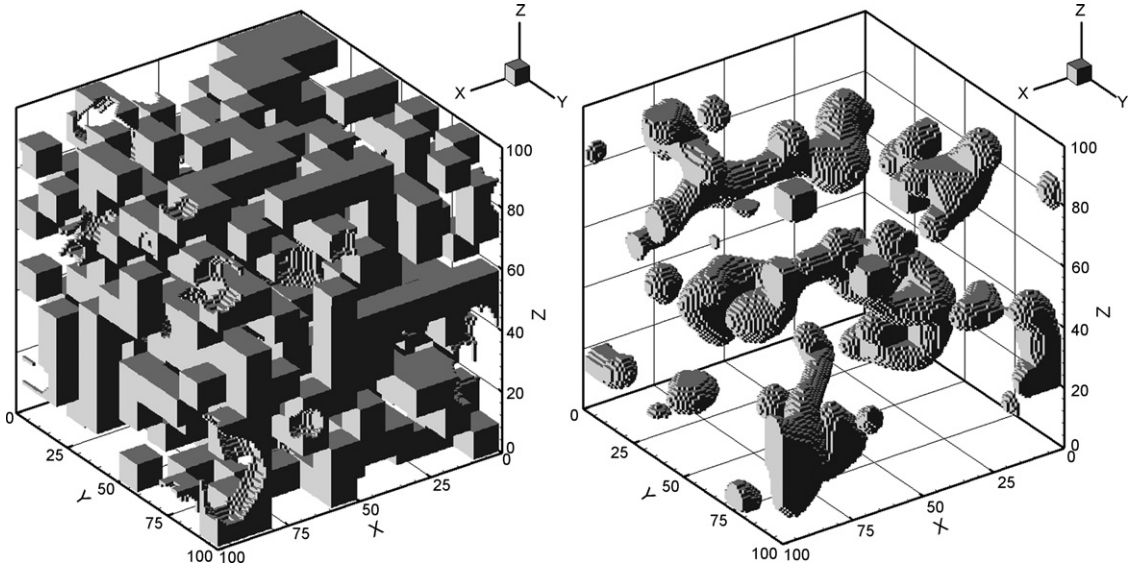

Fig. 19. Phase distribution patterns in 3D pore networks of the wetting phase (left panel) and the non-wetting phase (right panel) when $M = 10$ and $S_w = 0.8$. The solid is not shown in these figures. $D = 0.05$, $\theta = 175^\circ$, $G = 1.0\,e^{-7}$, $\varepsilon = 0.53$, and $\kappa = 10^{-4}$.

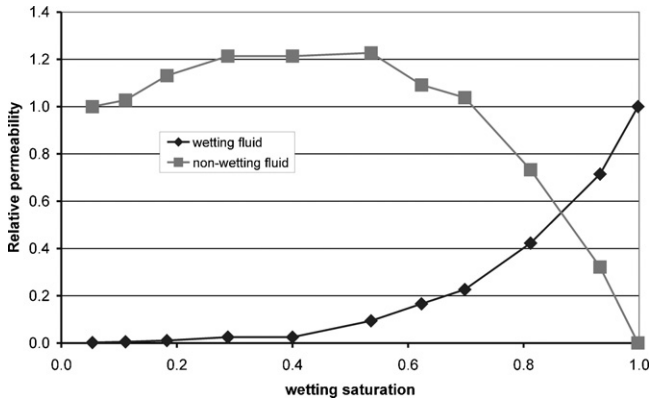

Fig. 20. Relative permeabilities when $M = 10$ in the 3D pore network. $D = 0.05$, $\theta = 175°$, $G = 1.0\,e^{-7}$, $\varepsilon = 0.53$, and $\kappa = 10^{-4}$.

The apparent relative permeabilities for both phases with respect to the wetting saturation are shown in Fig. 24. The relative permeabilities of both phases are less than one, as expected when the wetting phase is more viscous than the non-wetting phase. However, the relative permeability curve of the non-wetting phase is qualitatively different than the same curve for $M = 0.1$ for the flow between parallel plates (Section 4). This should be attributed to the fact that neither of the phases is very strongly wetting the solid and also to the presence of the disordered porous medium.

Under the conditions assumed in this paper, namely relatively high Capillary numbers [38], both fluids co-exist in most pores and there is strong viscous coupling between them. The wetting fluid moves along the solid surface and the non-wetting phase is not generally in contact with the solid, but it flows in the central part of the void surrounded by the wetting fluid.

The effect of viscous coupling on the apparent relative permeability of the wetting phase is more significant within the pore network than between the parallel plates examined in Section

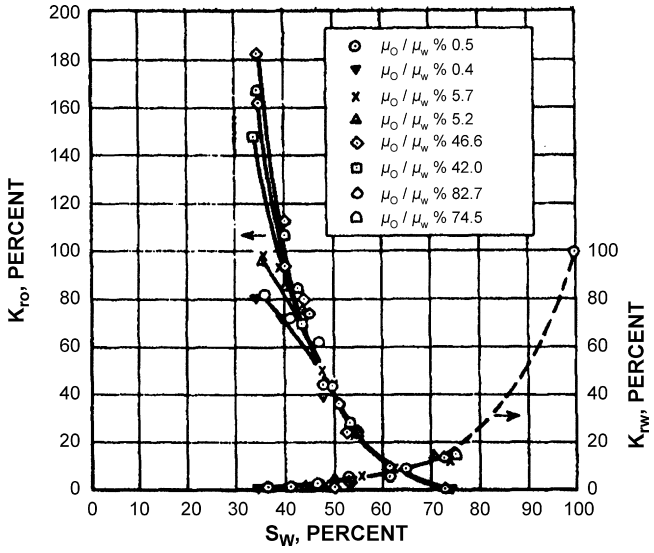

Fig. 21. Relative permeabilities of water and oil in low permeability sandstone (from Ref. [36]). For values of $M > 1$, the relative permeability of takes values greater than 1.

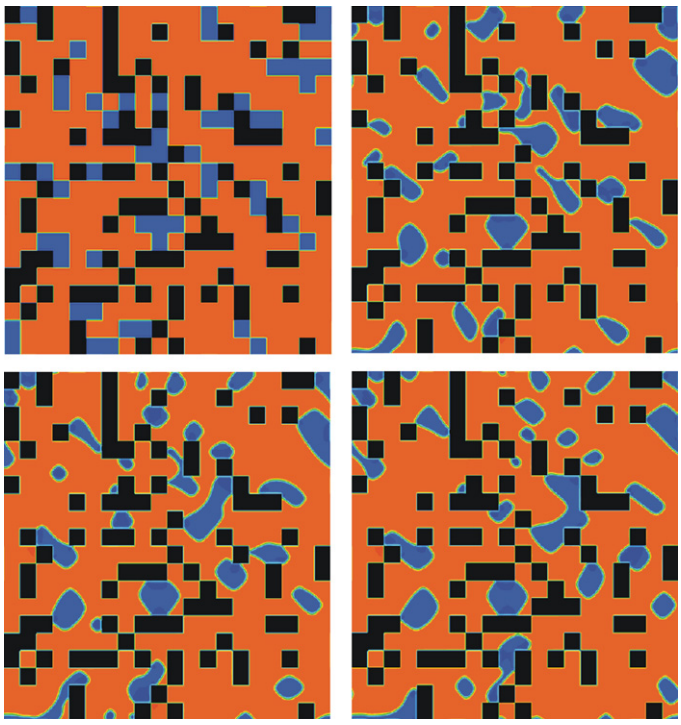

Fig. 22. Phase distribution patterns in 2D pore networks at different times ($t = 0$, 100,000, 200,000, 300,000δt) when the wetting phase is the more viscous phase (red color) $M = 0.1$ at $S_w = 0.8$. The less viscous non-wetting phase is shown in blue color. $D = 0.65$, $\theta = 55°$, $G = 1.0\,e^{-7}$, $\varepsilon = 0.77$, and $\kappa = 10^{-4}$. (For interpretation of the references to colour in this figure legend, the reader is referred to the web version of the article.)

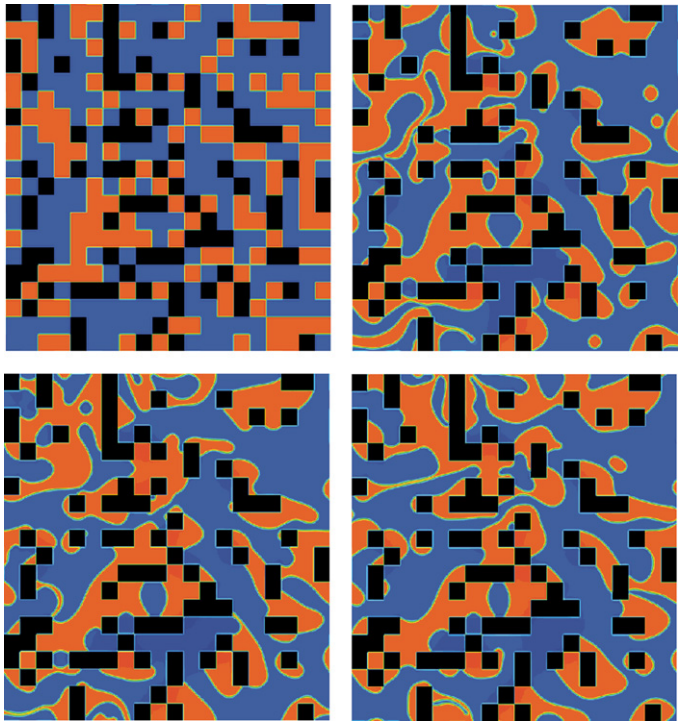

Fig. 23. Phase distribution patterns at different times ($t = 0$, 100,000, 200,000, 300,000δt) when the wetting phase is the more viscous phase (red color) $M = 0.1$ at $S_w = 0.4$. The less viscous non-wetting phase is shown in blue color. $D = 0.65$, $\theta = 55°$, $G = 1.0\,e^{-7}$, $\varepsilon = 0.77$, and $\kappa = 10^{-4}$. (For interpretation of the references to colour in this figure legend, the reader is referred to the web version of the article.)

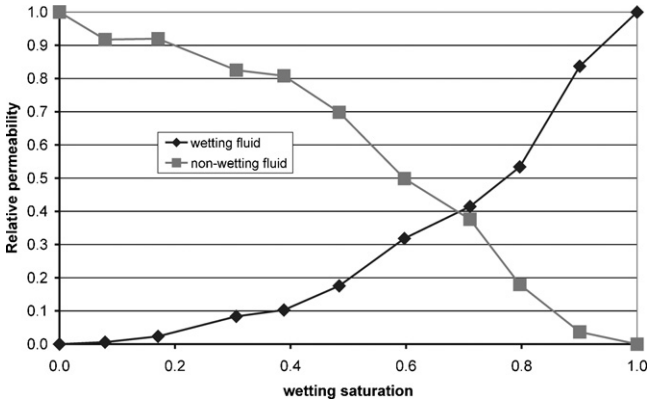

Fig. 24. Relative permeabilities in 2D pore networks when $M = 0.1$. $D = 0.65$, $\theta = 55^\circ$, $G = 1.0\,e^{-7}$, $\varepsilon = 0.77$, and $\kappa = 10^{-4}$.

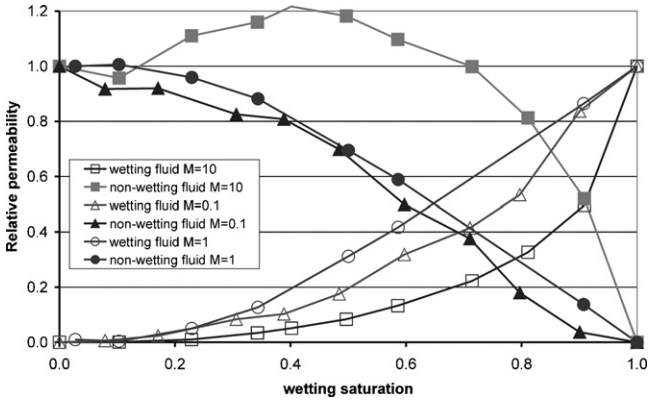

Fig. 25. Relative permeabilities for various values of M in the 2D pore network considered in this study. $G = 1.0\,e^{-7}$, $\varepsilon = 0.77$, and $\kappa = 10^{-4}$.

4 (compare Figs. 11 and 25). On the other hand, the lubricating effect on the non-wetting phase becomes less important in the porous medium due to the disordered nature of the pore space. The relative permeability of the non-wetting phase does not exceed 1.2 in the pore network when $M = 10$, while for the flow between parallel plates it takes values much greater than 1.

7. Conclusions

In this study we consider two-phase flow in irregular square and cubic pore networks using the immiscible two-phase lattice Boltzmann model proposed by He et al. [1], where the interface thickness is maintained between 3 and 4 lattice units. This unique feature of the He et al. model makes it ideal for flows in pores and cavities with a size of only a few lattice units.

By considering a set of appropriate boundary conditions for the index function, we account for the effect of wettability at solid–fluid interfaces and capillary effects within the pore space. It is shown that steady state contact angle is a linear function of the density value assigned to the solid sites.

The proposed model is applied to study of the relative permeabilities with respect to the wetting saturation and the viscosity ratio in pore networks. We find that non-wetting phase permeabilities may exceed single phase permeabilities under certain flow conditions (relatively high values of the Capillary number and low contact angles), when viscous forces control the movement of the interface and when the wetting phase is less viscous than the wetting phase. This indicates strong viscous coupling between the phases flowing in the same pores and also "lubrication" by a thin wetting phase film covering the pore walls.

To the best of our knowledge this is the first study that viscous coupling in two-phase flow through porous media has been modeled using a LB approach. Our results show that the LB model used in this study is an ideal tool for modeling immiscible flow in porous media, due both to its ability to incorporate complicated boundary conditions at the pore walls and also capture the physical aspects of the flow in the bulk and the interfaces.

Acknowledgements

The authors acknowledge the help and computational resources provided by the Barcelona Supercomputing Center (BSC) and the Centre de Supercomputació de Catalunya (CESCA) under the EC funded HPC-Europa project (RII3-CT-2003-506079).

Appendix A. Calculation of relative permeabilities for immiscible two phase flow between parallel plates

We consider the permeability of each phase in two phase flow between two parallel plates at distance $2L$ as shown in Fig. 9. The length and depth of the plates are both infinite.

The relative permeability $k_{r,i}$ of each phase i at a fixed saturation S_i is defined as; $k_{r,i} = Q_i(S_i)/Q_i(S_i = 1)$, where Q_i is the flow rate of phase i.

We assume that the wetting phase is located over the plates at $a < |x| < L$ and the non-wetting phase is located at $0 < |x| < a$.

The local velocity within the wetting phase reads

$$u(x) = \frac{F}{2\nu_w\rho_w}(L^2 - x^2) = \frac{FL^2}{2\nu_w\rho_w}\left(1 - \frac{x^2}{L^2}\right) \tag{A.1}$$

Assuming single phase flow of the wetting phase in the slit, the flow rate of the wetting phase is

$$\begin{aligned} Q_{w,max} &= 2N\int_{x=0}^{L} u(x)\,dx = 2N\int_{x=0}^{L} u(x)\,dx \\ &= 2N\frac{FL^2}{2\nu_w\rho_w}\int_0^L \left(1 - \frac{x^2}{L^2}\right)dx = \frac{2}{3}\frac{NFL^3}{\nu_w\rho_w} \end{aligned} \tag{A.2}$$

where N is the depth of the plates.

The relative permeability at saturation S_w is

$$k_{r,w} = \frac{Q_w(S_w)}{Q_{w,max}} = \frac{1}{Q_{w,max}}\int_a^L \frac{FL^2}{2\nu_w\rho_w}\left(1 - \frac{x^2}{L^2}\right)dx \tag{A.3}$$

Given that $S_w = (L - a)/L = 1 - (a/L)$, Eq. (A.3) reads;

$$k_{r,w} = \frac{1}{2}S_w^2(3 - S_w) \tag{A.4}$$

Eq. (A.4) shows that the relative permeability of the wetting phase is independent of the viscosity ratio M.

The local velocity in the non-wetting phase is

$$u(x) = \frac{F}{2\nu_{\mathrm{w}}\rho_{\mathrm{w}}}(L^2 - a^2) + \frac{F}{2\nu_{\mathrm{nw}}\rho_{\mathrm{nw}}}(a^2 - x^2) \tag{A.5}$$

Assuming single phase flow of the non-wetting phase in the slit, the flow rate of the non-wetting phase is

$$Q_{\mathrm{nw,max}} = \frac{2}{3}\frac{NFL^3}{\nu_{\mathrm{nw}}\rho_{\mathrm{nw}}} \tag{A.6}$$

The relative permeability at saturation $S_{\mathrm{nw}} = 1 - S_{\mathrm{w}}$ is

$$k_{\mathrm{r,nw}} = \frac{Q_{\mathrm{nw}}(1 - S_{\mathrm{w}})}{Q_{\mathrm{nw,max}}} = \frac{1}{Q_{\mathrm{nw,max}}}\int_{x=0}^{a}\frac{F}{2\nu_{\mathrm{w}}\rho_{\mathrm{w}}}(L^2 - a^2)\,\mathrm{d}x + \frac{1}{Q_{\mathrm{nw,max}}}\int_{0}^{a}\frac{F}{2\nu_{\mathrm{nw}}\rho_{\mathrm{nw}}}(a^2 - x^2)\,\mathrm{d}x \tag{A.7}$$

$$k_{\mathrm{r,nw}} = S_{\mathrm{nw}}\left[\frac{3}{2}M + S_{\mathrm{nw}}^2\left(1 - \frac{3}{2}M\right)\right] \tag{A.8}$$

where $M = \nu_{\mathrm{nw}}\rho_{\mathrm{nw}}/\nu_{\mathrm{w}}\rho_{\mathrm{w}}$.

References

[1] X. He, R. Zhang, S. Chen, G.D. Doolen, Phys. Fluids 11 (1999) 1143–1152.
[2] J.L. Lage, B.V. Antohe, J. Fluids Eng. 122 (2000) 619–625.
[3] F.A.L. Dullien, Porous Media: Fluid Transport and Pore Structure, Academic Press, San Diego, 1992.
[4] S. Whitaker, Trans. Porous Media 1 (1986) 105–125.
[5] F. Kalaydjian, Trans. Porous Media 5 (1990) 215–229.
[6] C. Pan, M. Hilpert, C.T. Miller, Water Resour. Res. 40 (2004) W01501.
[7] H. Li, C. Pan, C.T. Miller, Phys. Rev. E 72 (2005) 026705.
[8] P. Grosfils, J.P. Boon, J. Chin, E.D. Boek, Phil. Trans. R. Soc. Lond. A 362 (2004) 1723–1734.
[9] X. Nie, Y.-H. Qian, G.D. Doolen, S. Chen, Phys. Rev. E 58 (1998) 6861–6864.
[10] X. He, S. Chen, R. Zhang, J. Comp. Phys. 152 (1999) 642–663.
[11] R. Zhang, X. He, G.D. Doolen, S. Chen, Adv. Water Res. 24 (2001) 461–478.
[12] T. Lee, C.-L. Lin, J. Comp. Phys. 206 (2005) 16–47.
[13] S. Chen, G.D. Doolen, Annu. Rev. Fluid Mech. 30 (1998) 329–364.
[14] A.J.C. Ladd, R. Verberg, J. Stat. Phys. 104 (2001) 1191–1251.
[15] S. Succi, The Lattice-Boltzmann Equation, Oxford University Press, New York, 2001.
[16] R.R. Nourgaliev, T.N. Dinh, T.G. Theophanous, D. Joseph, Int. J. Multiphase Flow 29 (2003) 117–169.
[17] U. Frisch, B. Hasslacher, Y. Pomeau, Phys. Rev. Lett. 56 (1986) 1505–1508.
[18] C. Pan, J.F. Prins, C.T. Miller, Comp. Phys. Comm. 158 (2004) 89–105.
[19] A.K. Gunstensen, D.H. Rothman, S. Zaleski, G. Zanetti, Phys. Rev. A 43 (1991) 4320–4327.
[20] D.H. Rothman, J. Keller, J. Stat. Phys. 52 (1988) 1119–1127.
[21] X. He, G.D. Doolen, J. Stat. Phys. 107 (2002) 309–328.
[22] X. Shan, H. Chen, Phys. Rev. E 47 (3) (1993) 1815–1819.
[23] X. Shan, H. Chen, Phys. Rev. E 49 (4) (1994) 2941–2948.
[24] N.S. Martys, H. Chen, Phys. Rev. E 53 (1996) 743–750.
[25] M.S. Swift, W.R. Osborn, J.M. Yeomans, Phys. Rev. Lett. 75 (1995) 830–833.
[26] M.S. Swift, E. Orlandini, W.R. Osborn, J.M. Yeomans, Phys. Rev. E 54 (1996) 5041–5052.
[27] A.N. Kalarakis, V.N. Burganos, A.C. Payatakes, Phys. Rev. E 65 (2002) 056702.
[28] A.N. Kalarakis, V.N. Burganos, A.C. Payatakes, Phys. Rev. E 67 (2003) 016702.
[29] X. He, X. Shan, G.D. Doolen, Phys. Rev. E 57 (1998) R13–R16.
[30] P. Raiskinmaki, A. Shakib-Manesh, A. Jasberg, A. Koponen, J. Merikoski, J. Timonen, J. Stat. Phys. 107 (2002) 143–158.
[31] P.L. Bhatnagar, E.P. Gross, M. Krook, Phys. Rev. 94 (1954) 511–525.
[32] S. Chapman, T.G. Cowling, The Mathematical Theory of Non-Uniform Gases, Cambridge University Press, 1990.
[33] N.F. Carnahan, K.S. Starling, J. Chem. Phys. 51 (2) (1969) 635–636.
[34] J.S. Rowlinson, B. Widom, Molecular Theory of Capillarity, Dover Publications, 2003.
[35] S. Bekri, P.M. Adler, Int. J. Multiphase Flow 28 (2002) 665–697.
[36] A.S. Odeh, Petrol. Trans.-AIME 216 (1959) 346–353.
[37] P.S. Pacheco, Parallel Programming with MPI, Morgan Kaufmann Publishers, San Francisco, 1997.
[38] J.F. Le Romancer, C. Touboul, C. Zarcone, J. Fluid Mech. 189 (1988) 165–187.
[39] P.A. Goode, T.S. Ramakrishnan, AIChE J. 39 (7) (1993) 1124–1134.
[40] R. Ehrlich, Trans Porous Media 11 (1993) 201–218.